

Chapter 5

Zeolite-Templated Carbon: Anomalous Methane Adsorption

5.1 Introduction

5.1.1 Background

For effective energy storage by physical adsorption, a high total capacity (corresponding to a large number of binding sites) is necessary for high potential delivery. Additionally, the characteristic binding energies of the sorbent-adsorbate interactions are crucial to the practical deliverable capacity because the storage tank must be cycled between two finite pressures, and the amount stored in the system at the lower bound (e.g., 0.3 MPa) should ideally be low. The optimal material for physisorptive energy storage can be assumed to have a high binding energy that is constant with increased loading. For hydrogen, the average enthalpy of adsorption across a wide variety of carbon materials (activated carbon, nanofibers, aerogels, templated-carbons, etc.) is $4\text{-}6 \text{ kJ (mol H}_2\text{)}^{-1}$,^{1, 2} which is not significantly higher than the average thermal energy at 298 K and limits their effective use to cryogenic temperatures. Physical adsorption of methane is much stronger, typically $12\text{-}20 \text{ kJ mol}^{-1}$ ^{1, 2} and near-ambient temperature applications for methane storage are promising.

In microporous carbonaceous materials, the pore structure and surface chemistry are the characteristics that offer the potential to adjust the thermodynamic properties of adsorption. Boron- and nitrogen-doped materials have shown promise in exhibiting higher enthalpies of adsorption.³⁻⁵ However, as in pure carbon-based materials, the enthalpy declines rapidly with loading. A more effective approach for tuning the thermodynamics of adsorption is by controlling the pore-size distribution and mean pore width to achieve optimal binding interactions. Theoretical models of adsorption in graphitic slit pores show that pore-widths corresponding to three molecular diameters of the adsorptive gas are ideal for maximizing adsorbate-adsorbate interactions and increasing the total energy of adsorption.⁶⁻⁸ However, adsorption measurements on engineered graphene-scaffolds⁹ and other microporous materials^{10, 11} have never shown an appreciably increasing binding energy in the high surface coverage regime.

Template carbonization is an effective technique for producing carbonaceous materials with exceptionally large specific surface area and controlled porosity.^{12, 13} Zeolite-templated carbons (ZTCs) are microporous, amorphous carbon materials with extremely high surface area and a periodic array of pores complementary to the structure of the zeolite used in the template-carbonization synthesis, and are extensively described in Chapter 4. We synthesized numerous ZTCs with varying properties, and here we present a study of their thermodynamic properties during methane adsorption, a secondary application that is well suited to this particular class of materials. A key property of faujasite-templated ZTCs, such as ZTC-3, is the sharp pore-size distribution centered at 1.2 nm, markedly differing from other microporous carbons

which typically have a wide distribution of pore-widths. While the nature of the microstructure of carbonaceous materials has not been previously reported to have a significant effect on their adsorptive capacities for methane,¹⁴ pore widths in ZTCs approach the optimal value suggested by theoretical studies to be 1.14 nm.^{6, 7} Recent calculations of methane adsorption on metal-organic framework CPO-27-Mg, a crystalline material with well-characterized adsorption sites within small (~1.1 nm) cages, show that strong adsorbate-adsorbate interactions play an important role in the enthalpy of methane adsorption, resulting in a 15% increase in excess capacity at near 298 K.¹⁵ By performing detailed adsorption measurements of methane adsorption in ZTC-3 at 13 temperatures between 238-526 K, we find that in fact the precise conditions for enhanced enthalpy of adsorption from lateral interactions have been achieved, an effect that had been elusive to experimental groups up until the time of this study. The implications are significant since ZTCs have both extremely high surface area and well-adapted porosity for methane adsorption, giving them a strong advantage over typical carbons in deliverable methane capacity at high pressure.

5.1.2 Materials

Zeolite-templated carbon, ZTC-3, was synthesized by the impregnation of zeolite NaY with poly-furfuryl alcohol, undergoing a propylene CVD step at 700°C, and carbonization was performed at 900°C. The template was removed by dissolution in HF. Details of the synthesis, and the important steps for attaining high template fidelity, are found in Section 4.2, following the standard procedure.¹⁶ For comparison, two other commercial activated carbons were also investigated: CNS-201, a modest surface area

carbon with extremely narrow micropores, and MSC-30, a superactivated carbon with extremely high surface area that is often measured as a standard. These materials were degassed at 250°C under vacuum to < 0.1 mPa before use. The surface and pore characteristics of the materials used in this study are given in Table 5.1.

Table 5.1: Material properties of activated carbons CNS-201 and MSC-30, and zeolite-templated carbon ZTC-3.

Material	Skeletal Density [◊] (g mL ⁻¹)	Bulk Density ^{◊◊} (g mL ⁻¹)	BET Surface Area (m ² g ⁻¹)	DR Micropore Volume (mL g ⁻¹)	247 K CH ₄ Capacity [†] (mmol g ⁻¹)	298 K CH ₄ Capacity ^{††} (mmol g ⁻¹)	~523 K CH ₄ Capacity ^{†††} (mmol g ⁻¹)
CNS-201	2.1	0.50	1095 ± 8	0.45	7.45	5.98	2.48
MSC-30	2.1	0.27	3244 ± 28	1.54	20.2	14.5	5.16
ZTC-3	1.8	0.18	3591 ± 60	1.66	20.5	14.1	4.76

[◊] Skeletal density measured using He at 298 K between 0-3 MPa. ^{◊◊} Bulk density measured on maximum packing. [†] Measured at 247 K and Gibbs excess maximum pressure. ^{††} Measured at 298 K and Gibbs excess maximum pressure. ^{†††} Measured at 526, 521, and 518 K for CNS-201, MSC-30, and ZTC-3, respectively, at 10 MPa.

The pore-size distribution in CNS-201, obtained by the non-localized density functional theory (NLDFT) method, contains 3 peaks, at 0.54 nm, 0.80 nm, and 1.18 nm, with 50%, 20%, and 15% of the pore volume in each, respectively (see Figure 5.1). MSC-30 contains a broad distribution of pore-widths between 0.6-3.5 nm and 40% of the pore volume is contained in pores > 2.1 nm in width. The distribution of pores in ZTC-3 is

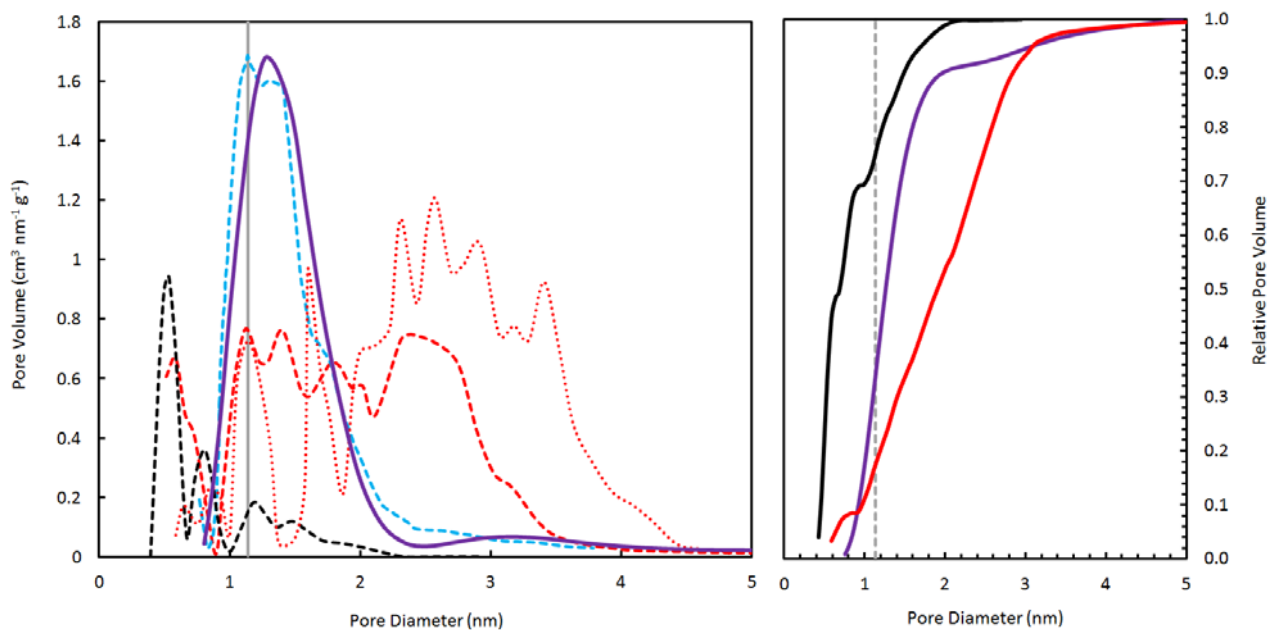


Figure 5.1. The pore-size distribution (left) and relative filling (right) of CNS-201 (black), MSC-30 (red), ZTC “P7(2)-H” (blue), and ZTC-3 (purple), calculated by the NLDFT method.

characterized by a single sharp peak centered at 1.2 nm, with > 90% of the pore volume having a pore width between 0.85-2.0 nm. This regularity of pore-size in ZTC-3 was confirmed by x-ray diffraction (XRD), which shows a sharp peak centered at $2\theta = 6^\circ$ (see Figure 4.4), and transmission electron microscopy (TEM) which shows a periodic spacing of diffraction contrast corresponding to pores of width 1 nm (see Figure 4.8). Skeletal densities of the samples were measured by helium pycnometry; the activated carbons have 2.1 g mL^{-1} , consistent with a wide variety of carbonaceous materials¹⁷, while ZTC-3 has a lower skeletal density (1.8 g mL^{-1} , consistent with other ZTCs¹⁶) presumably due to increased hydrogen terminations (a detailed discussion can be found in Section 4.5.1).

5.2 Methane Adsorption

5.2.1 High-Pressure Experiments

Methane adsorption isotherms at all temperatures were measured with a volumetric Sieverts apparatus, commissioned and verified for accurate measurements up to 10 MPa.¹⁸⁻²⁰ The sample was submerged in a chiller bath for sub-ambient temperature isotherms. For high temperatures, the sample was placed inside a cylindrical copper heat exchanger and wrapped with insulated fiberglass heating tape. A PID controller and K-type thermocouples were used to maintain a consistent temperature throughout measurement; fluctuations were less than ± 0.1 K at low temperature and no higher than ± 0.4 K at high temperatures. The system was leak tested up to 10 MPa and showed a maximum leak rate of 7.0×10^{-6} mol h⁻¹ of CH₄. In Equation 3.1, this corresponds to a maximum leak of $k \sim 10^{-8}$ s⁻¹ which is negligible for short time measurement.²¹ The total inner volume of the apparatus was 66 mL.

Prior to methane adsorption measurements, 0.3-1.5 g of sample was loaded and degassed at 250°C under vacuum to < 0.1 mPa for 12 h. Two adsorption runs using research-grade methane (99.999%) were performed at each temperature and the data were combined for thermodynamic analysis. Multiple adsorption/desorption cycles were also performed at various temperatures to assure full reversibility of methane physisorption in the complete temperature and pressure regime of study and to test the precision of the experiments. Error between cycles was $< 1\%$ of the measured value. For example, three independent (non-consecutive) hydrogen adsorption/desorption cycles in ZTC-3 at 298 K are shown in Figure 5.2. The sample was degassed once before cycling

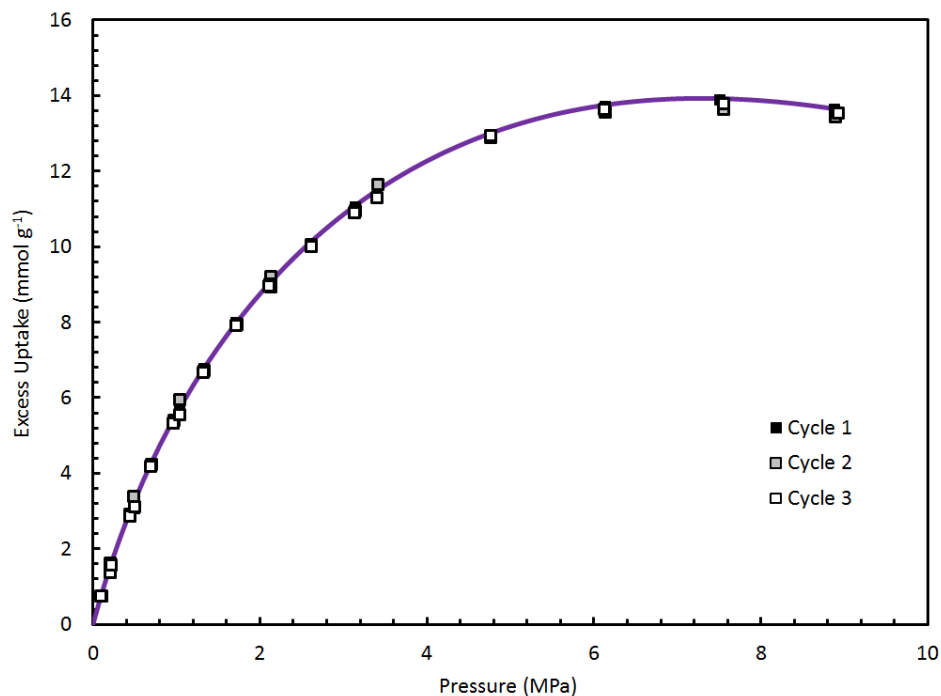


Figure 5.2. Equilibrium excess adsorption/desorption isotherms of methane on ZTC-3 at 298 K. Three cycles are shown, including adsorption and desorption points, displaying complete reversibility of uptake in these materials and showing typical precision between independent measurements.

but was not further treated between cycles. Equilibrium adsorption isotherms at 238, 298, and ~523 K are shown in Figure 5.3 for a direct comparison between the materials.

The complete set of methane adsorption isotherms on CNS-201, MSC-30, and ZTC-3 are shown in Figures 5.4-6. The excess maximum is similar for ZTC-3 and MSC-30 at room temperature, but slightly higher for MSC-30: 14.5 mmol g⁻¹ at 8 MPa. While excess adsorption increases faster for MSC-30 at pressures between 0-0.8 MPa, uptake in ZTC-3 increases fastest between 0.8-5.7 MPa. Gravimetric uptake in CNS-201 is substantially less at all temperatures due to its low specific surface area. The highest measured excess uptake of this study is for ZTC-3 at 238 K: 22.1 mmol g⁻¹ (26.2 wt%) at 4.7 MPa,

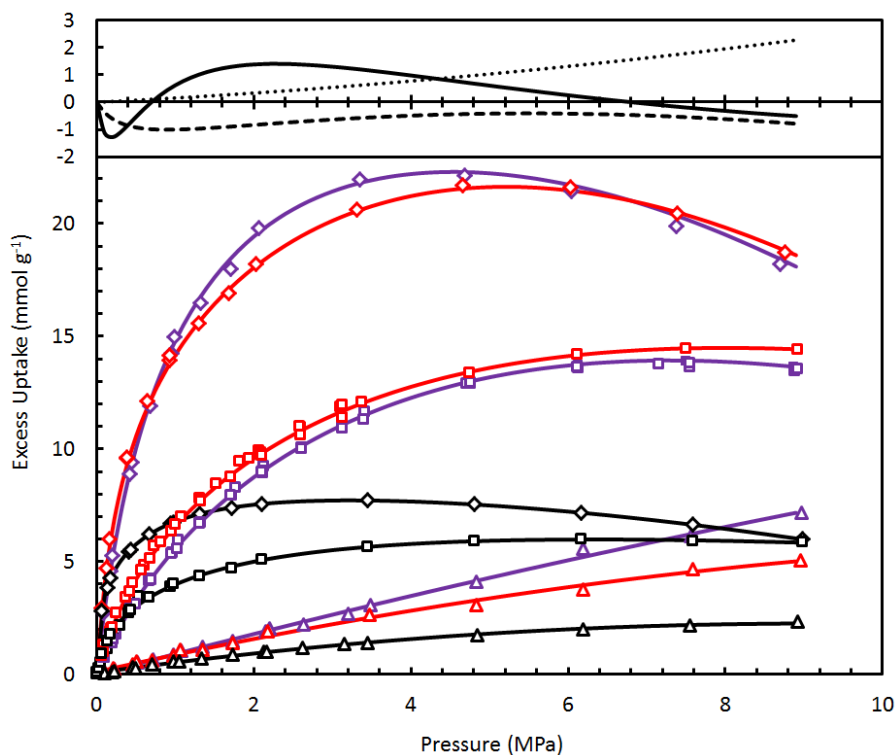


Figure 5.3. Comparison of equilibrium excess adsorption isotherms of methane on CNS-201 (black), MSC-30 (red), and ZTC-3 (purple) at 238 K (diamond), 298 K (square), and ~523 K (triangle). The difference between ZTC-3 and MSC-30 is shown at the top: 238 K (full line), 298 K (dashed line), ~523 K (dotted line).

despite a gentler initial increase at low pressure. Interestingly, the excess uptake in ZTC-3 is also greater than MSC-30 at high temperatures although neither reaches a maximum between 0-9 MPa. These values correspond to a significant enhancement of deliverable methane capacity over pure compressed gas storage. At all temperatures, methane uptake in ZTC-3 is characterized by a gradual initial rise and delayed increase at pressures between 0.2-2 MPa, leading to higher eventual methane capacity than MSC-30, a material of comparable specific surface area.

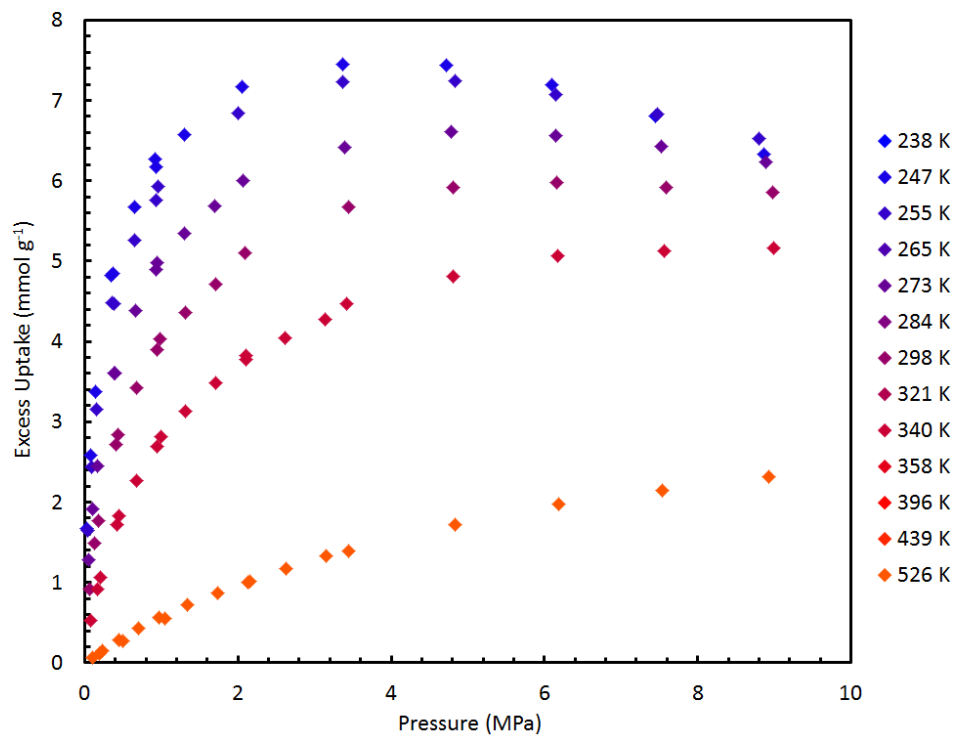


Figure 5.4. Equilibrium adsorption isotherms of methane on CNS-201 between 0-9 MPa.

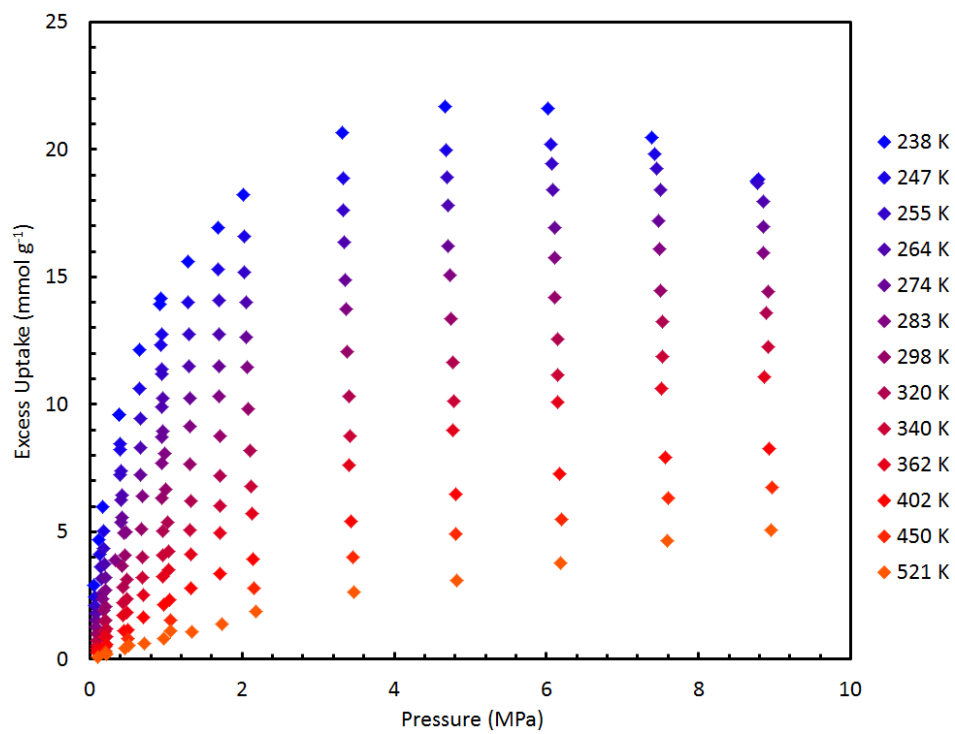


Figure 5.5. Equilibrium adsorption isotherms of methane on MSC-30 between 0-9 MPa.

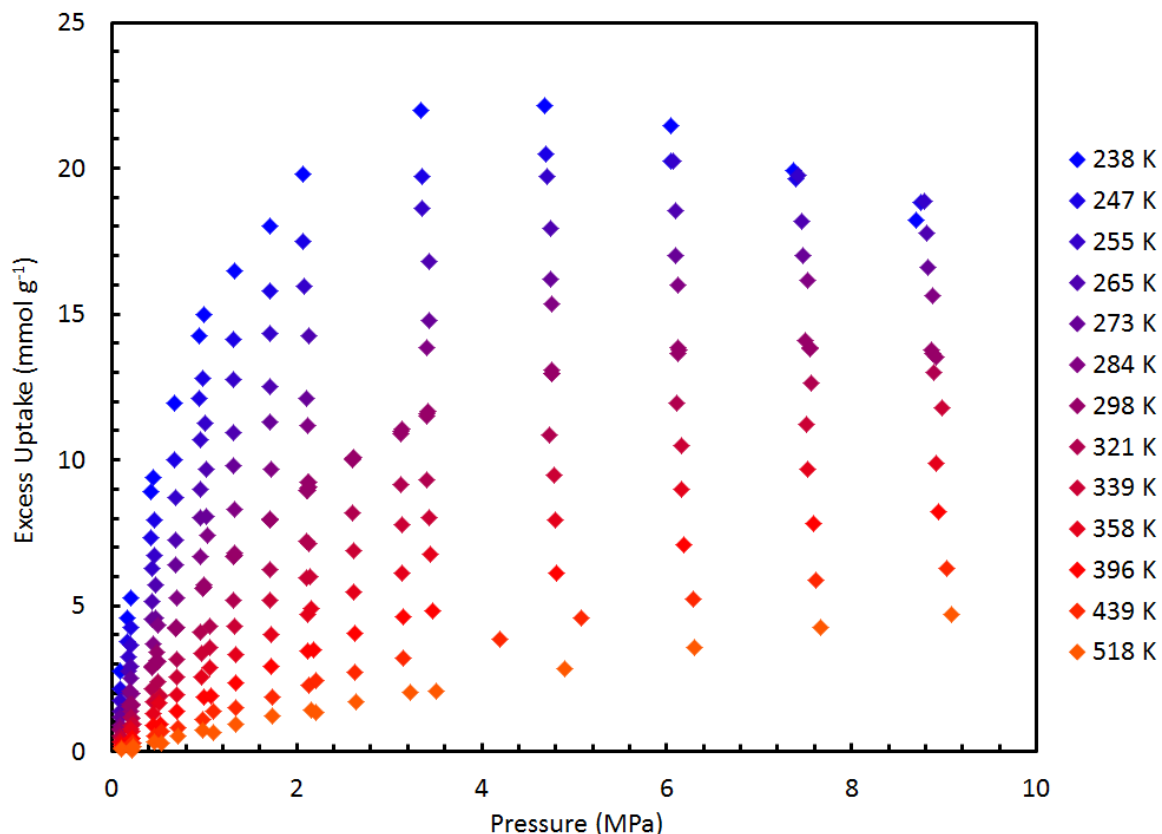


Figure 5.6. Equilibrium adsorption isotherms of methane on ZTC-3 between 0-9 MPa.

5.2.2 Fitting the Experimental Data

The experimental adsorption isotherms were fitted with the generalized-Langmuir equation, following the procedure detailed in Section 2.5. This is a general and very robust approach that allows the adsorption volume be an independent parameter of the fitting equation. The generalized-Langmuir fit was compared to other models, specifically the Unilan²² and Langmuir-Freundlich type fitting equations, and better fits were given by the generalized-Langmuir equation. This can be considered a model-independent approach (as in Equation 2.47) or an approach to determine the absolute

quantity of adsorption (as in Equation 2.50). The minimum number of independent parameters is desired, and for the materials in this study, we find that $i = 2$ yields satisfying results. The optimized parameters are given in Table 5.2.

Least squares fits of the methane adsorption isotherms (on CNS-201, MSC-30, and ZTC-3) to the generalized-Langmuir equation are shown in Figure 5.7, the fitted excess adsorption (left) and calculated absolute adsorption (right) at all temperatures measured. The goodness of fit was satisfactory across the entire range of temperature and pressure for all three samples, with a residual sum of squares of $<0.04 \text{ mmol g}^{-1}$ per data point.

5.2.3 Trends

The maximum in excess adsorption measured in this study at 298 K scales linearly with the specific surface area of the materials studied, a relationship analogous to “Chahine’s rule”²³ for the surface excess maximum of hydrogen at 77 K, consistent with the reported linear trend for methane uptake at 3.5 MPa and 298 K (see Figure 5.8).¹⁴ The fit parameters can also be compared with the properties of the materials studied, shown in Figure 5.9. The scaling parameter n_{max} is proportional to the number of binding sites, found to be well approximated by the BET specific surface area. The maximum volume of the adsorbed layer, V_{max} , is also proportional to surface area for the activated carbons, although it is limited by the pore-width. The maximum volume of the adsorbed layer in ZTC-3 corresponds to half of the mean pore diameter that is characteristic of the material: a thickness of 0.6 nm.

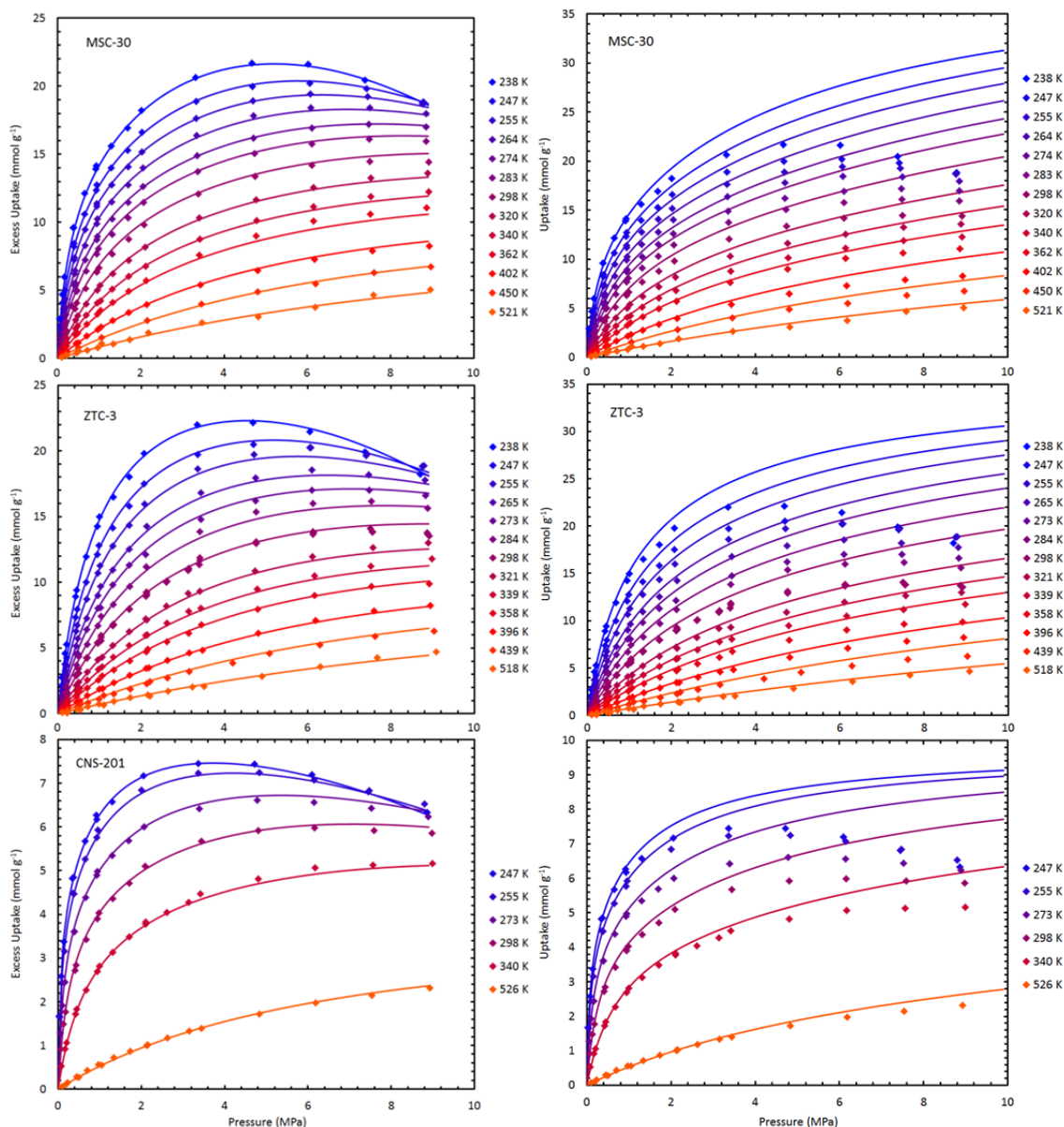


Figure 5.7. The fitted experimental data for MSC-30 (top), ZTC-3 (middle), and CNS-201 (bottom): excess uptake (left) and absolute uptake (right) at temperatures from 238-526 K (blue to orange). The diamonds are measured (excess) uptake.

Table 5.2: Least-squares minimized fit parameters of the generalized-Langmuir equation for methane adsorption on CNS-201, MSC-30, and ZTC-3 between 238-526 K.

Material	n_{\max} (mmol g ⁻¹)	V_{\max} (mL g ⁻¹)	α	A_1 (K ^{1/2} MPa ⁻¹)	E_1 (kJ mol ⁻¹)	A_2 (K ^{1/2} MPa ⁻¹)	E_2 (kJ mol ⁻¹)
CNS-201	9.77	0.49	0.58	0.061	17.2	0.0044	16.4
MSC-30	41.0	2.30	0.70	0.068	13.4	0.0046	12.9
ZTC-3	35.6	2.04	0.46	0.059	11.6	0.00018	20.4

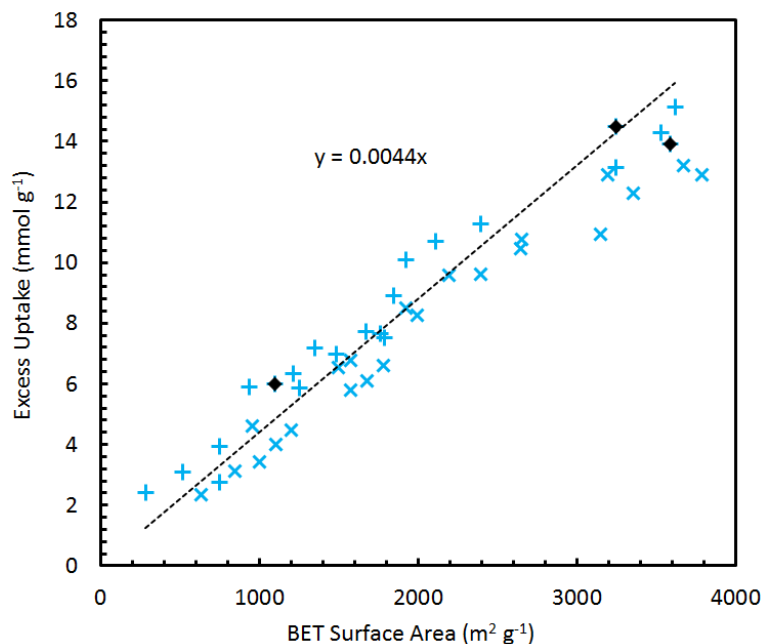


Figure 5.8. Equilibrium excess adsorption uptake of methane as a function of BET surface area, reported at the excess maximum at 298 K for CNS-201, MSC-30, and ZTC-3 (black diamonds). A + indicates a reported value from the literature.²⁵ A × indicates a reported value of the BET monolayer capacity from the literature.²⁷

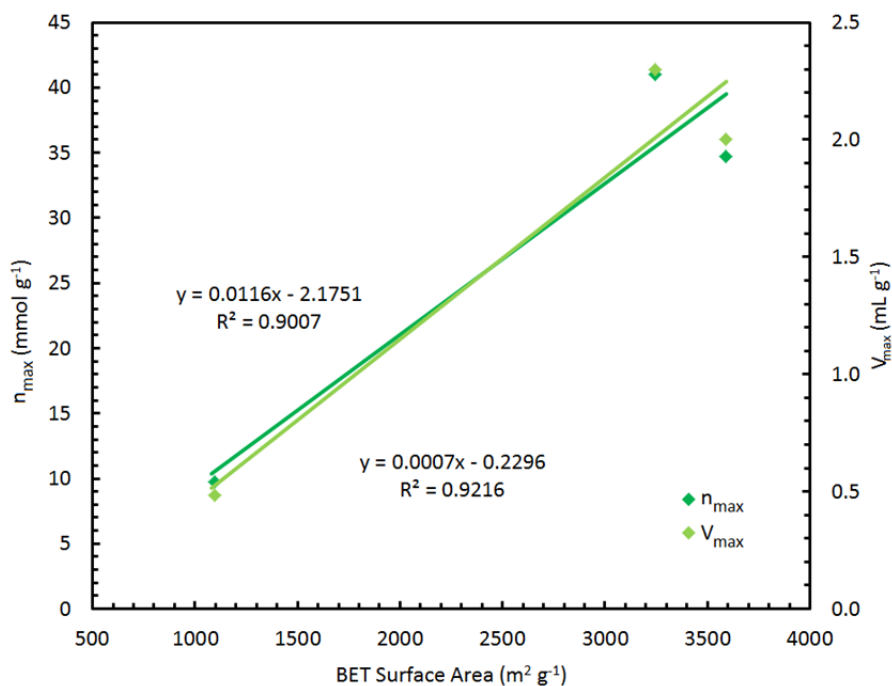


Figure 5.9. The dependence of fit parameters n_{\max} and V_{\max} on BET surface area for CNS-201, MSC-30, and ZTC-3.

5.3 Enthalpy of Adsorption

The thermodynamic quantity of interest for adsorbent materials is the differential enthalpy of adsorption,²⁴ ΔH_{ads} , often obtained by the isosteric method and reported as the positive value q_{st} , the isosteric heat of adsorption.²⁵ We refer to the quantity as “enthalpy” but use the following (positive) definition:

$$q_{st} = -\Delta H_{ads}(n_a) = T \left(\frac{\partial P}{\partial T} \right)_{n_a} (v_g - v_a)$$

Equation 5.1

It is necessary to use this general form of the Clausius-Clapeyron relationship for methane adsorption at high pressure due to the significant non-ideality of methane gas-state properties, preventing the usual van't Hoff analysis. The real (REFPROP)²⁶ bulk gas density was used and the adsorbed density was approximated as limited by liquid methane (see Section 2.3.3), giving significantly different results than by assuming ideal gas density. The isosteric enthalpy of adsorption of methane on CNS-201, MSC-30, and ZTC-3 at the temperatures measured is shown in Figure 5.10. A detailed analysis of alternative methods of the calculation of adsorption enthalpy is given in Chapter 2.

The Henry's law values of the isosteric enthalpy of adsorption for CNS-201, MSC-30, and ZTC-3 are 18.0-19.3, 14.4-15.5, and 13.5-14.2 kJ mol⁻¹, respectively. The same temperature dependence of this value is found for both activated carbons: +4.1 J mol⁻¹ K⁻¹. The Henry's law values from 238-518 K for ZTC-3 depend nonlinearly on temperature, indicating significantly different thermodynamics of methane adsorption in this range. At low temperatures the trend is negative (-16 J mol⁻¹ K⁻¹ at 247 K), and

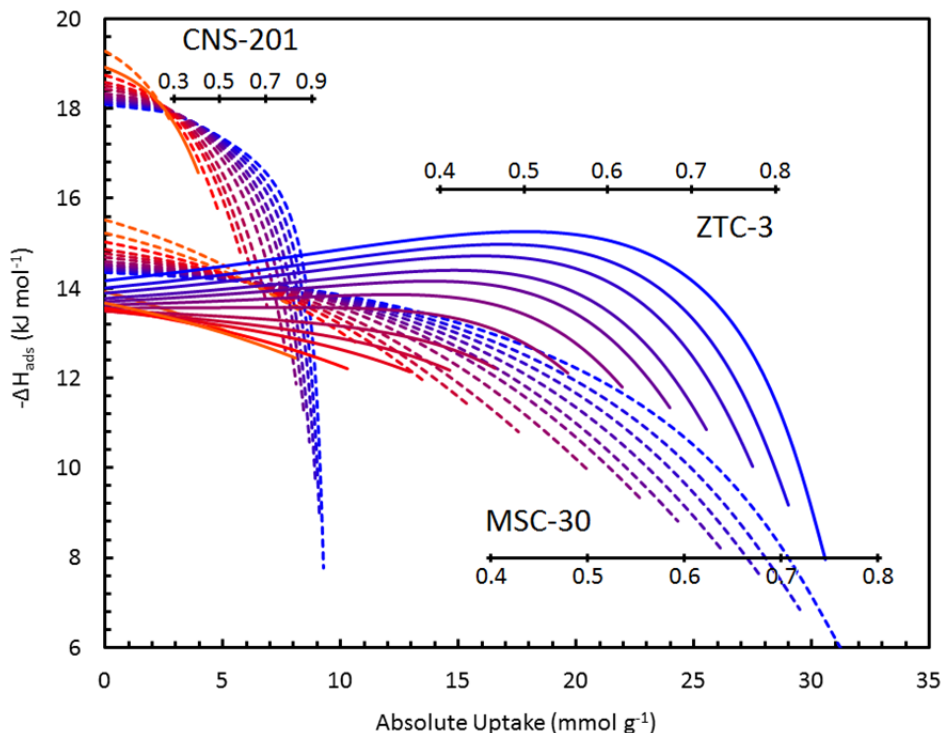


Figure 5.10. Isosteric enthalpy of adsorption of methane on CNS-201, MSC-30, and ZTC-3 from 238-523 K (color indicates the temperature from low to high as blue to red). Scale bars of the fractional site occupancy (specific to each material) are inset.

then increases toward that of the activated carbons (reaching $+3.0 \text{ J mol}^{-1} \text{ K}^{-1}$ at 450 K).

The characteristics of methane adsorption as a function of fractional site occupancy, ϑ , in the activated carbons (CNS-201 and MSC-30) are typical of other carbon materials, gradually decreasing with increased uptake. On the contrary, the dependence of the isosteric enthalpy of adsorption on site occupancy in ZTC-3 increases with ϑ at all temperatures, from 238-518 K. The enthalpy increases to a maximum at $\vartheta = 0.5\text{-}0.6$, and then declines rapidly at high uptake. The rapid decline is similar in all three materials, occurring at $\vartheta > 0.7$, and is a result of high, non-ideal density in the high-pressure gas; an ideal gas approximation would be completely invalid in this high-pressure regime.

5.4 Entropy of Adsorption

The molar differential entropy of adsorption, while less relevant to engineering applications, is a readily accessible quantity of adsorption via the isosteric method following the procedure in Section 2.3.2. The pressure dependence of the entropy of the pure gas phase can be obtained from the REFPROP database. Together, these quantities can be used to calculate the entropy of methane in the adsorbed phase, given by:

$$S_a(P, T) = \Delta S_{ads}(P, T) + S_g(P, T)$$

Equation 5.2

The entropy of the adsorbed phase, S_a , on CNS-201, MSC-30, and ZTC-3 is shown in Figure 5.11, where the reference state is the normal boiling point of methane, 111.5 K at 0.1 MPa. While all three materials show a similar change in entropy with increased uptake, there are notable differences between that for the small-pore materials (CNS-201 and ZTC-3) and MSC-30, which has pores ranging in width up to > 4 nm. The high-pressure entropy of methane adsorbed on CNS-201 and ZTC-3 at 238 K resembles that at the reference state rather closely, despite being ~100 K above those conditions, indicating a liquid-like behavior of the adsorbed layer. This is, however, a subtle difference and MSC-30 may show a similar effect at slightly lower temperatures. The rise in entropy at the highest pressures measured is not well understood, but corresponds to the sharp decrease in enthalpy shown in Figure 5.10. This regime corresponds to filling the last adsorption sites available, and could reflect some contribution from disorder in the filling of those sites.

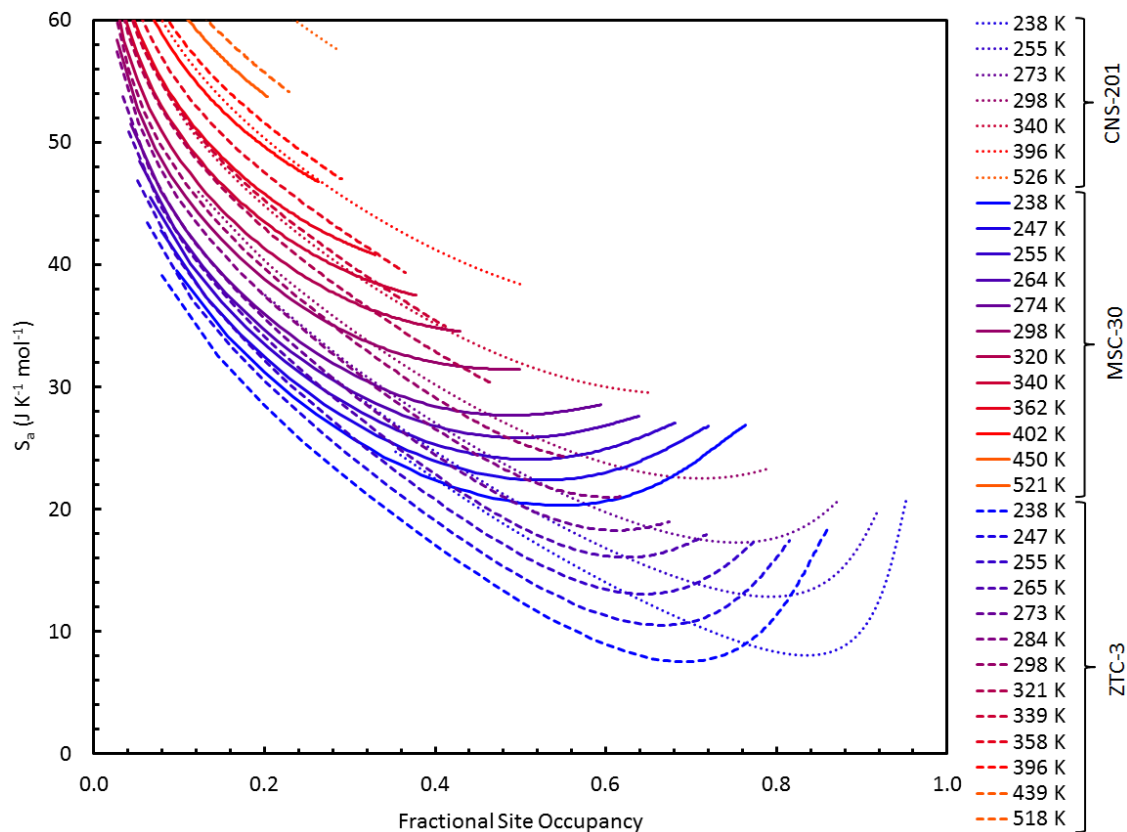


Figure 5.11. Entropy of methane in the adsorbed phase as a function of fractional site occupancy.

5.5 Discussion

The increasing isosteric enthalpy of adsorption in ZTC-3 is anomalous compared to previous experimental reports of methane adsorption on carbon. However, it is consistent with calculations of methane adsorption in graphitic slit pores of fixed width^{6, 27} where methane-methane interactions between adsorption sites are expected to have a significant role.²⁸ Its rise of 1.2 kJ mol^{-1} at 298 K corresponds to a 10% increase, remarkably consistent with recent calculations of the relative contribution of lateral

interactions to the enthalpy of adsorption of methane on CPU-27-Mg¹⁵ and on molecular sieves.¹⁰ The possibility of entropic contributions (e.g., from additional vibrational modes of bound CH₄ molecules) cannot be ruled out and further investigation with deuterated molecules would be interesting.

Surface homogeneity is not a requirement for increased interactions between binding sites, but would certainly enhance the measurable effect on the enthalpy of adsorption at high uptake. The material properties of ZTC-3, such as a narrow distribution of pore-width, periodic pore-spacing, and high content of sp² hybridized carbon (as characterized by NMR and numerous other techniques²⁹), suggest a high binding site homogeneity is probable. The average distance between adsorbed methane molecules (approximated as the square root of the BET surface area per molecule) at the surface excess maximum was the same in all three materials in this study (e.g., 0.5 nm at 238 K) and well within the distance applicable to attractive lateral interactions.

We therefore assert that lateral interactions play a major role in methane adsorption on ZTC-3, overcoming any heterogeneities in the surface and causing a significant overall rise in enthalpy of adsorption as site occupancy increases, though it is not possible to determine the precise magnitude of this effect since surface homogeneity is unknown.

5.6 Conclusions

An increasing (or even constant) isosteric enthalpy of adsorption over a large regime of temperature and pressures is a highly desirable characteristic of an adsorbent

material. It benefits deliverable storage capacity because a large fraction of the maximum adsorption capacity is contained at pressures above the lower bound of useful storage (e.g., $P_f = 0.3$ MPa for delivery to a fuel cell) rather than below it, as in materials with a high initial binding energy that decreases with loading. Due to the flexibility of the template-carbonization synthesis, the pore-width can be adapted to other adsorptive gases by simply changing the template, making this a highly promising approach for the design of adsorbent materials for gases with attractive intermolecular forces. Indeed, the deliverable gravimetric methane capacities of ZTC-3 at temperatures near ambient are among the highest of any reported carbonaceous materials, a direct result of enhancing thermodynamic performance in the surface coverage regime of interest ($P > P_f$).

5.7 References

- (1) S. K. Bhatia and A. L. Myers, 'Optimum conditions for adsorptive storage', *Langmuir*, **22**, 1688-1700 (2006).
- (2) A. Chakraborty, B. B. Saha, K. C. Ng, S. Koyama, and K. Srinivasan, 'Theoretical insight of physical adsorption for a single component adsorbent + adsorbate system: II. The Henry region', *Langmuir*, **25**, 7359-7367 (2009).
- (3) T. C. M. Chung, Y. Jeong, Q. Chen, A. Kleinhammes, and Y. Wu, 'Synthesis of microporous boron-substituted carbon (B/C) materials using polymeric precursors for hydrogen physisorption', *J. Am. Chem. Soc.*, **130**, 6668-6669 (2008).
- (4) Z. Jin, Z. Z. Sun, L. J. Simpson, K. J. O'Neill, P. A. Parilla, Y. Li, N. P. Stadie, C. C. Ahn, C. Kittrell, and J. M. Tour, 'Solution-phase synthesis of heteroatom-substituted carbon scaffolds for hydrogen storage', *J. Am. Chem. Soc.*, **132**, 15246-15251 (2010).
- (5) Y. Xia, G. S. Walker, D. M. Grant, and R. Mokaya, 'Hydrogen storage in high surface area carbons: experimental demonstration of the effects of nitrogen doping', *J. Am. Chem. Soc.*, **131**, 16493-16499 (2009).
- (6) K. R. Matranga, A. L. Myers, and E. D. Glandt, 'Storage of natural gas by adsorption on activated carbon', *Chem. Eng. Sci.*, **47**, 1569-1579 (1992).
- (7) D. Nicholson, 'Simulation studies of methane transport in model graphite micropores', *Carbon*, **36**, 1511-1523 (1998).
- (8) D. Lozano-Castello, D. Cazorla-Amoros, A. Linares-Solano, and D. F. Quinn, 'Influence of pore size distribution on methane storage at relatively low pressure: preparation of activated carbon with optimum pore size', *Carbon*, **40**, 989-1002 (2002).

- (9) Z. Jin, W. Lu, K. J. O'Neill, P. A. Parilla, L. J. Simpson, C. Kittrell, and J. M. Tour, 'Nano-engineered spacing in graphene sheets for hydrogen storage', *Chem. Mater.*, **23**, 923-925 (2011).
- (10) M. M. K. Salem, P. Braeuer, M. Szombathely, M. Heuchel, P. Harting, K. Quitzsch, and M. Jaroniec, 'Thermodynamics of high-pressure adsorption of argon, nitrogen, and methane on microporous adsorbents', *Langmuir*, **14**, 3376-3389 (1998).
- (11) P. Bénard and R. Chahine, 'Determination of the adsorption isotherms of hydrogen on activated carbons above the critical temperature of the adsorbate over wide temperature and pressure ranges', *Langmuir*, **17**, 1950-1955 (2001).
- (12) T. Kyotani, 'Control of pore structure in carbon', *Carbon*, **38**, 269-286 (2000).
- (13) H. Nishihara and T. Kyotani, 'Templated nanocarbons for energy storage', *Adv. Mater.*, **24**, 4473-4498 (2012).
- (14) Y. Sun, C. Liu, W. Su, Y. Zhou, and L. Zhou, 'Principles of methane adsorption and natural gas storage', *Adsorption*, **15**, 133-137 (2009).
- (15) K. Sillar and J. Sauer, 'Ab initio prediction of adsorption isotherms for small molecules in metal-organic frameworks: the effect of lateral interactions for methane/CPO-27-Mg', *J. Am. Chem. Soc.*, doi: 10.1021/ja307076t (2012).
- (16) H. Nishihara, P. X. Hou, L. X. Li, M. Ito, M. Uchiyama, T. Kaburagi, A. Ikura, J. Katamura, T. Kawarada, K. Mizuuchi, and T. Kyotani, 'High-pressure hydrogen storage in zeolite-templated carbon', *J. Phys. Chem. C*, **113**, 3189-3196 (2009).
- (17) B. Panella, M. Hirscher, and S. Roth, 'Hydrogen adsorption in different carbon nanostructures', *Carbon*, **43**, 2209-2214 (2005).
- (18) T. P. McNicholas, A. Wang, K. O'Neill, R. J. Anderson, N. P. Stadie, A. Kleinhammes, P. Parilla, L. Simpson, C. C. Ahn, Y. Wang, Y. Wu, and J. Liu, 'H₂ storage in microporous carbons from PEEK precursors', *J. Phys. Chem. C*, **114**, 13902-13908 (2010).
- (19) J. J. Purewal, H. Kabbour, J. J. Vajo, C. C. Ahn, and B. Fultz, 'Pore size distribution and supercritical hydrogen adsorption in activated carbon fibers', *Nanotechnology*, **20**, 204012 (2009).
- (20) N. P. Stadie, J. J. Purewal, C. C. Ahn, and B. Fultz, 'Measurements of hydrogen spillover in platinum doped superactivated carbon', *Langmuir*, **26**, 15481-15485 (2010).
- (21) T. Kiyobayashi, H. T. Takeshita, H. Tanaka, N. Takeichi, A. Züttel, L. Schlapbach, and N. Kuriyama, 'Hydrogen adsorption in carbonaceous materials – how to determine the storage capacity accurately', *J. Alloys Compd.*, **330-332**, 666-669 (2002).
- (22) J. Purewal, D. Liu, A. Sudik, M. Veenstra, J. Yang, S. Maurer, U. Müller, and D. J. Siegel, 'Improved hydrogen storage and thermal conductivity in high-density MOF-5 composites', *J. Phys. Chem. C*, **116**, 20199-20212 (2012).
- (23) E. Poirier, R. Chahine, and T. K. Bose, 'Hydrogen adsorption in carbon nanostructures', *Int. J. Hydrogen Energ.*, **26**, 831-835 (2001).
- (24) S. Sircar, R. Mohr, C. Ristic, and M. B. Rao, 'Isostatic heat of adsorption: theory and experiment', *J. Phys. Chem. B*, **103**, 6539-6546 (1999).
- (25) F. Rouquerol, J. Rouquerol, and K. S. W. Sing, *Adsorption by powders and porous solids: principles, methodology, and applications*, Academic Press, San Diego (1999).
- (26) E. W. Lemmon, M. L. Huber, and M. O. McLinden, 'NIST standard reference database 23: reference fluid thermodynamic and transport properties – REFPROP', Number Version 8.0 in Standard Reference Data Program (2007).
- (27) R. F. Cracknell, P. Gordon, and K. E. Gubbins, 'Influence of pore geometry on the design of microporous materials for methane storage', *J. Phys. Chem.*, **97**, 494-499 (1993).
- (28) S. A. Al-Muhtaseb and J. A. Ritter, 'Roles of surface heterogeneity and lateral interactions on the isosteric heat of adsorption and adsorbed phase heat capacity', *J. Phys. Chem. B*, **103**, 2467-2479 (1999).
- (29) N. P. Stadie, J. J. Vajo, R. W. Cumberland, A. A. Wilson, C. C. Ahn, and B. Fultz, 'Zeolite-templated carbon materials for high-pressure hydrogen storage', *Langmuir*, **28**, 10057-10063 (2012).